Calculation of two-photon absorption by nanocrystals of CsPbBr3

Blundell, S. A.; Nguyen, T. P. T.; Guet, Claude

2021

Blundell, S. A., Nguyen, T. P. T. & Guet, C. (2021). Calculation of two-photon absorption by nanocrystals of CsPbBr3. Physical Review B, 103(4), 045415-.
https://dx.doi.org/10.1103/PhysRevB.103.045415

https://hdl.handle.net/10356/151090

https://doi.org/10.1103/PhysRevB.103.045415

Calculation of two-photon absorption by nanocrystals of $CsPbBr_3$

S. A. Blundell,[1,*] T. P. T. Nguyen,[1,†] and C. Guet[2,3,‡]
[1]*Université Grenoble Alpes, CEA, CNRS, IRIG, SyMMES, F-38000 Grenoble, France*
[2]*Energy Research Institute, Nanyang Technological University, 637141 Singapore*
[3]*School of Materials Science and Engineering, Nanyang Technological University, 639798 Singapore*

(Received 5 October 2020; revised 6 December 2020; accepted 4 January 2021; published 15 January 2021)

We present calculations of the two-photon absorption cross section $\sigma^{(2)}(\omega)$ for nanocrystals (NCs) of the inorganic perovskite $CsPbBr_3$ for photon energies ω ranging from the absorption threshold at $2\omega \approx 2.3$ eV up to $2\omega = 3.1$ eV. The calculations employ a 4×4 $\mathbf{k} \cdot \mathbf{p}$ envelope-function model, with final-state excitons described in a self-consistent Hartree-Fock approximation. The $\mathbf{k} \cdot \mathbf{p}$ corrections to $\sigma^{(2)}(\omega)$ are found to be rather large, giving a reduction of about 30% in the cross section at the largest energies considered. The cross section is shown to be independent of polarization in the effective-mass approximation (EMA), but including $\mathbf{k} \cdot \mathbf{p}$ corrections leads to a small difference in $\sigma^{(2)}(\omega)$ between circular and linear polarization, which rises to about 16% at $2\omega = 3.1$ eV. The theoretical cross section follows closely a power-law dependence on NC size, $\sigma^{(2)}(\omega) \propto L^{\alpha}$, with theoretical exponents $\alpha = 3.4$ (EMA) or $\alpha = 3.2$ (4×4 $\mathbf{k} \cdot \mathbf{p}$ model), in excellent agreement with experiment. The dominant contribution to the exponent α is shown to be the number of final-state excitons per unit energy. Measured values of the absolute (normalized) cross section $\sigma^{(2)}(\omega)$ show a large spread of values, differing by as much as a factor of 25 for some NC sizes. Our calculations strongly favor a group of measurements at the lower end of the reported range of $\sigma^{(2)}(\omega)$.

DOI: 10.1103/PhysRevB.103.045415

I. INTRODUCTION

In 2015, a new class of semiconductor nanocrystal (NC) materials emerged having excellent light-emitting properties, NCs of inorganic lead halide perovskites $CsPbX_3$ (X = Cl, Br, and I) [1,2]. These NCs are free of blinking and display strong fluorescence with high color purity, the emission frequency being tunable over the entire visible spectrum by varying the size of the NCs and the halide composition X [1–3]. The quantum yields approach unity [4]. These outstanding emission properties have led to important applications to light-emitting diodes [5,6], lasers [7,8], and single-photon sources [9].

Absorption by these NCs has also been studied extensively, including measurements of the one-photon [10–14], two-photon [10,12–17], and up to five-photon [15] absorption spectra. Multiphoton absorption by NCs has important technological applications to three-dimensional (3D) biomedical imaging, as the absorption of several infrared photons with reemission at a shorter wavelength gives improved penetration depth and low biological damage, combined with good spatial confinement [18]. Other applications of multiphoton absorption include nonlinear photonic devices for information and communication technologies [19]. NCs of inorganic lead halide perovskites are highly attractive for such applications on account of their outstanding optoelectronic properties, combined with a low-cost solution-processed synthesis [1].

Two-photon and multiphoton absorption has been most extensively studied experimentally in $CsPbBr_3$. However, the reported values of the two-photon cross section in $CsPbBr_3$ [10,12–17] show large disagreements among themselves, differing by as much as a factor of 25 for some NC sizes. Meanwhile, to our knowledge there has so far been no theoretical treatment of multiphoton absorption by NCs of lead halide perovskites. To help clarify this issue, therefore, we present in this paper calculations of the two-photon absorption spectra of NCs of $CsPbBr_3$.

The paper is organized as follows. We start in Sec. II A by outlining our 4×4 $\mathbf{k} \cdot \mathbf{p}$ envelope-function model for NCs of $CsPbBr_3$, together with a self-consistent Hartree-Fock (HF) treatment of a confined exciton. We used a similar approach in an earlier study [20] of one-photon absorption by NCs of $CsPbBr_3$ and $CsPbI_3$. The detailed formalism for two-photon absorption is then discussed in Sec. II B. Although NCs of $CsPbBr_3$ are cuboid [1], for reasons of computational efficiency, we use a spherical "quasicubic" confining potential for the main parts of the calculation. This formalism is discussed in Sec. II B 1. To gauge the accuracy of the quasicubic potential, we also consider in Sec. II B 2 two-photon absorption by a cubic NC, assuming the effective-mass approximation (EMA) and noninteracting electron and hole states. These approximations allow us to derive an analytical formula for the two-photon absorption cross section.

The applications to NCs of $CsPbBr_3$ are described in Sec. III. First, in Sec. III A, we give the material parameters assumed for $CsPbBr_3$. Next, in Sec. III B, we discuss some theoretical aspects of the two-photon absorption process in $CsPbBr_3$. These include the role of $\mathbf{k} \cdot \mathbf{p}$ corrections (which

*steven.blundell@cea.fr
†phuctan3108@gmail.com
‡cguet@ntu.edu.sg

turn out to be quite large), the accuracy of the quasicubic spherical potential, and the polarization dependence of the two-photon cross section. Our theoretical two-photon cross sections are then compared to the available data for $CsPbBr_3$ in Sec. III C, and our conclusions are given in Sec. IV. Throughout, all formulas are given in atomic units: $\hbar = |e| = m_0 = 4\pi\epsilon_0 = 1$.

II. FORMALISM

A. Envelope-function k · p model

We consider a system of carriers (electrons and holes) confined by a mesoscopic potential $V_{\rm ext}(\mathbf{r})$. The carrier wave functions are obtained from a multiband $\mathbf{k}\cdot\mathbf{p}$ envelope-function formalism, with the intercarrier Coulomb interactions screened by the dielectric constant $\varepsilon_{\rm in}$ of the NC material. (Our approach is described in more detail in Refs. [20–22].) The system Hamiltonian in the space of electron envelope functions is

$$H = \sum_{ij}\{i^\dagger j\}\langle i|h_{\mathbf{k}\cdot\mathbf{p}} + V_{\rm ext}|j\rangle + \frac{1}{2}\sum_{ijkl}\{i^\dagger j^\dagger lk\}\langle ij|g_{12}|kl\rangle, \tag{1}$$

where g_{12} is the long-range Coulomb interaction

$$g_{12} = \frac{1}{\varepsilon_{\rm in}|\mathbf{r}_1 - \mathbf{r}_2|}, \tag{2}$$

and $h_{\mathbf{k}\cdot\mathbf{p}}$ is a $\mathbf{k}\cdot\mathbf{p}$ Hamiltonian describing the bulk band structure. The notation $\{i_1^\dagger i_2^\dagger \ldots j_1 j_2 \ldots\}$ in Eq. (1) indicates a normally ordered product of creation (and annihilation) operators for the electron envelope states $i_1, i_2, \ldots$ (and $j, j_2, \ldots$) in the valence and conduction bands included in the calculation.

NCs of $CsPbBr_3$ are generally cuboid [1]. In parts of the calculation, we take the confining potential $V_{\rm ext}$ to be a cubic well with infinite walls and edge length L:

$$V_{\rm ext}^{\rm cube}(\mathbf{r}) = \begin{cases} 0, & \text{if } 0 < x, y, z < L \\ \infty, & \text{otherwise.} \end{cases} \tag{3}$$

In the EMA, noninteracting states (electron or hole) in the above potential are described by three positive integers (n_x, n_y, n_z),

$$\psi_{n_x n_y n_z}(\mathbf{r}) = \sqrt{\frac{8}{L^3}}\sin\left(\frac{n_x\pi x}{L}\right)\sin\left(\frac{n_y\pi y}{L}\right)\sin\left(\frac{n_z\pi z}{L}\right), \tag{4}$$

with (kinetic or confinement) energy

$$\epsilon_{\rm cube}(n_x, n_y, n_z) = \frac{\pi^2}{2m_\lambda^* L^2}\left(n_x^2 + n_y^2 + n_z^2\right), \tag{5}$$

where m_λ^* is the effective mass of the corresponding electron or hole band.

In other parts of the calculation (including the HF treatment of the electron-hole Coulomb interaction and higher-order $\mathbf{k}\cdot\mathbf{p}$ corrections), we instead choose the basis states i, j, etc., appearing in Eq. (1) to be those appropriate for a spherical confining potential. As in our previous work [20,21], this is done for reasons of computational efficiency because only the radial dimension of the basis states then needs to be handled numerically. For this purpose, we take the confining potential to be a "quasicubic" spherical well [20,21,23]

$$V_{\rm ext}^{\rm sph}(r) = \begin{cases} 0, & \text{if } r < R \\ \infty, & \text{otherwise.} \end{cases} \tag{6}$$

The radius R is related to the edge length L of the corresponding cube by

$$R = L/\sqrt{3}, \tag{7}$$

which ensures that the noninteracting $1S$ ground state in the sphere (6) has the same energy as the noninteracting "$1S$-like" ($n_x = n_y = n_z = 1$) ground state in the cube (3). As shown in Refs. [20,21], other properties are well reproduced by the quasicubic spherical well (6). These include the Coulomb energy of the ground-state $1S_e$-$1S_h$ exciton and correlation energies (of the exciton, trion, and biexciton).

The bulk band-structure Hamiltonian $h_{\mathbf{k}\cdot\mathbf{p}}$ in Eq. (1) corresponds to a 4×4 $\mathbf{k}\cdot\mathbf{p}$ model including the $p_{1/2}$-like (R_6^-) conduction band (CB) and the s-like (R_6^+) valence band (VB) around the R point of the Brillouin zone [24,25]. For a spherical confining potential, the states in this model can be described in terms of basis vectors $|(lJ)FM_F\rangle$, in which the orbital angular momentum l of the envelope function couples to the Bloch angular momentum J of the band (here $J = \frac{1}{2}$ for both the CB and the VB) to give a total angular momentum F [26]. In the 4×4 $\mathbf{k}\cdot\mathbf{p}$ model, the CB and VB are coupled and the states have two components

$$|\eta FM_F\rangle = \frac{g_s(r)}{r}|(l, 1/2)FM_F\rangle + \frac{\bar{g}_p(r)}{r}|(\bar{l}, 1/2)FM_F\rangle. \tag{8}$$

The first component lies in the s-like VB, the second in the $p_{1/2}$-like CB; $g_s(r)$ and $\bar{g}_p(r)$ are radial functions. For a CB (electron) state, the second term is the large component, and the first term is a small component representing the admixture of the VB into the CB state due to the finite range of the confining potential $V_{\rm ext}$ and the $\mathbf{k}\cdot\mathbf{p}$ interaction. In a VB (hole) state, the roles of the large and small components are interchanged. The VB-CB coupling introduces nonparabolic terms into the bulk dispersion relation [26] and, in addition, the presence of the small components modifies the value of matrix elements (for example, Coulomb and electron-photon matrix elements [20,21]). In this way, $\mathbf{k}\cdot\mathbf{p}$ corrections are included in the calculation. We conventionally label states by the quantum numbers of the large component [for example, $1S_e$ for a CB state and $(1P_{1/2})_h$ for a VB state].

The electron-hole Coulomb interaction is treated at mean-field level by a self-consistent configuration-averaged HF approximation including exact exchange [20,21]. To evaluate the electron propagator required for the two-photon absorption amplitude (see Sec. II B), we construct a complete HF basis set, following the procedure of our earlier work [20,21]. The first step is to solve the HF equations self-consistently for the ground $1S_e$-$1S_h$ exciton, and the $1S_e$ and $1S_h$ orbitals are "frozen." Then, we compute excited (unoccupied) HF states up to a high-energy cutoff. We allow the excited electron (hole) states to experience the HF potential due to only the $1S_h$ hole ($1S_e$ electron) state. Since all electron states thus experience the same potential, they are automatically orthogonal, as required (and similarly for the hole states).

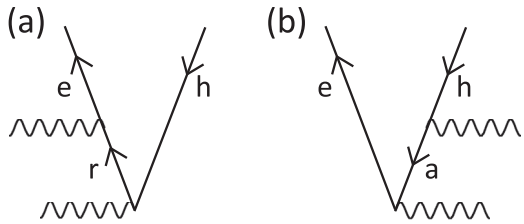

FIG. 1. Time-ordered diagrams for two-photon absorption from the ground state to a final-state exciton (e, h) (where e is an electron state and h a hole state). Diagrams (a) and (b) correspond to the amplitudes $\mathcal{M}_{eh}^{(a)}$ and $\mathcal{M}_{eh}^{(b)}$ in Eqs. (12) and (13), respectively.

B. Two-photon amplitude and cross section

We represent the laser as a classical electromagnetic wave with a vector potential $\mathbf{A}(\mathbf{r}, t) = (1/2)A_0[\mathbf{e}_\sigma e^{i(\mathbf{k}\cdot\mathbf{r}-\omega t)} + \mathbf{e}_\sigma^* e^{-i(\mathbf{k}\cdot\mathbf{r}-\omega t)}]$ far away from the NC, where $\mathbf{e}_\sigma$ is the complex polarization vector and σ denotes the polarization state. The electron-laser interaction inside the NC, within the electric-dipole approximation, is then

$$V_{\text{e-ph}}(t) = \tfrac{1}{2} f_\varepsilon A_0(\mathbf{e}_\sigma \cdot \mathbf{p} e^{-i\omega t} + \mathbf{e}_\sigma^* \cdot \mathbf{p} e^{i\omega t}), \tag{9}$$

where f_ε is the dielectric screening factor, which relates the amplitude of the vector potential inside the NC to its value at infinity. For spherical NCs (and within the electrostatic approximation), f_ε has the value [27]

$$f_\varepsilon^{\text{sph}} = \frac{3\varepsilon_{\text{out}}}{\varepsilon'_{\text{in}} + 2\varepsilon_{\text{out}}}, \tag{10}$$

where ε'_{in} is the optical dielectric constant of the material of the NC and ε_{out} is that of the surrounding medium. Note that ε'_{in} is not necessarily the same as the dielectric constant ε_{in} used to screen the Coulomb interactions in Eq. (2); the values used in our calculations are given in Sec. III A. As discussed in Ref. [20], based on the numerical calculations in Ref. [25], we expect the average value of f_ε for a cube to be within about 6% of the value $f_\varepsilon^{\text{sph}}$ for a sphere (10). Another numerical calculation [28] gives an average value of f_ε for a cube differing from $f_\varepsilon^{\text{sph}}$ by up to only 2%. In the following calculations, we shall take $f_\varepsilon = f_\varepsilon^{\text{sph}}$.

We wish to consider two-photon absorption from the ground state to a single-exciton final state (e, h). In time-dependent perturbation theory, the lowest-order (mean-field) amplitude for this process is given by the sum of the two terms shown in Fig. 1 [29,30],

$$\mathcal{M}_{eh} = \mathcal{M}_{eh}^{(a)} + \mathcal{M}_{eh}^{(b)}, \tag{11}$$

where

$$\mathcal{M}_{eh}^{(a)} = \sum_r^{(\text{CB})} \frac{\langle e|\mathbf{e}_\sigma \cdot \mathbf{p}|r\rangle\langle r|\mathbf{e}_\sigma \cdot \mathbf{p}|h\rangle}{\omega + \epsilon_h - \epsilon_r}, \tag{12}$$

$$\mathcal{M}_{eh}^{(b)} = -\sum_a^{(\text{VB})} \frac{\langle e|\mathbf{e}_\sigma \cdot \mathbf{p}|a\rangle\langle a|\mathbf{e}_\sigma \cdot \mathbf{p}|h\rangle}{\omega + \epsilon_a - \epsilon_e}. \tag{13}$$

Here, the sum over r is over states in the CB, and the sum over a is over states in the VB; ω is the laser frequency. We note that the first term in $V_{\text{e-ph}}(t)$ [Eq. (9)] leads to absorption, and the second to emission. For some purposes, it is convenient to combine $\mathcal{M}_{eh}^{(a)}$ and $\mathcal{M}_{eh}^{(b)}$ into a single term involving a sum over all states i in either the CB or the VB,

$$\mathcal{M}_{eh} = \sum_i^{(\text{CB+VB})} \frac{\langle e|\mathbf{e}_\sigma \cdot \mathbf{p}|i\rangle\langle i|\mathbf{e}_\sigma \cdot \mathbf{p}|h\rangle}{(\omega_{eh}/2) + \epsilon_h - \epsilon_i}, \tag{14}$$

which follows from Eqs. (12) and (13) if we assume that the laser is on resonance $2\omega = \omega_{eh} = \epsilon_e - \epsilon_h$. Note that $\mathcal{M}_{eh}^{(a)}$ and $\mathcal{M}_{eh}^{(b)}$ each involve a product of one interband and one intraband transition matrix element on the numerator.

The two-photon absorption rate Γ_{eh} to a final exciton (e, h) follows from Eqs. (9) and (11)–(13) to be (in units of photons absorbed per unit time)

$$\Gamma_{eh}(\omega) = \frac{8\pi^3}{n_{\text{out}}^2 c^2 \omega^2} f_\varepsilon^4 |\bar{\mathcal{M}}_{eh}|^2 I^2 \Delta_{eh}(\omega - \omega_{eh}/2), \tag{15}$$

where $|\bar{\mathcal{M}}_{eh}|^2$ is the amplitude squared (11) summed over all degenerate final states,

$$|\bar{\mathcal{M}}_{eh}|^2 = \sum_{M_e M_h} |\mathcal{M}_{eh}(M_e, M_h)|^2. \tag{16}$$

The indices M_e and M_h here (which enumerate the degenerate substates of e and h, respectively) take account of both the Bloch (band) degeneracy and any degeneracy in the envelope states arising from the symmetry of the confining potential. In Eq. (15), I is the laser fluence (in units of photons per unit area per unit time)

$$I = \frac{n_{\text{out}} c\, \omega}{8\pi} |A_0|^2, \tag{17}$$

$n_{\text{out}} = \sqrt{\epsilon_{\text{out}}}$ is the refractive index of the surrounding medium, ω_{eh} is the exciton energy, and $\Delta_{eh}(\omega - \omega_{eh}/2)$ is the line-shape function for the transition to (e, h), which is normalized as

$$\int_0^\infty \Delta_{eh}(\omega - \omega_{eh}/2)\, d\omega = 1. \tag{18}$$

The frequency-dependent two-photon absorption cross section to all possible single-exciton final states (e, h) is defined as $\tilde{\sigma}^{(2)}(\omega) = (1/I^2)\sum_{eh} \Gamma_{eh}(\omega)$, so that one has finally

$$\tilde{\sigma}^{(2)}(\omega) = \frac{8\pi^3}{n_{\text{out}}^2 c^2 \omega^2} f_\varepsilon^4 \sum_{eh} |\bar{\mathcal{M}}_{eh}|^2 \Delta_{eh}(\omega - \omega_{eh}/2). \tag{19}$$

Experimental results are usually presented instead in terms of a modified two-photon cross section

$$\sigma^{(2)}(\omega) = \frac{1}{f_\varepsilon^4} \tilde{\sigma}^{(2)}(\omega), \tag{20}$$

which is designed to remove the leading dependence on the environment, so that $\sigma^{(2)}(\omega)$ depends mostly only on the properties of the NC itself.[1] The units of $\sigma^{(2)}(\omega)$ are $\text{cm}^4\,\text{s photon}^{-1}$, with $1\ \text{GM} = 10^{-50}\ \text{cm}^4\,\text{s photon}^{-1}$.

[1]The environment still, in principle, modifies the electronic structure in the NC through the polarization charges induced on the surface of the NC by the dielectric mismatch with the environment, and through the spillout of the electron wave function into the environment. These small effects are neglected in this work.

In the next two subsections, we discuss special cases of these results relevant to spherical (quasicubic) and to cubic confining potentials.

1. Spherical potential

For states of spherical form (8), the two-photon amplitude (14) may be written

$$\mathcal{M}_{eh}(M_e, M_h) = \sum_i^{(\text{shells})} \mathcal{A}(M_e M_h; F_e F_h F_i; \mathbf{e}_\sigma) \times \frac{\langle F_e \| p^1 \| F_i\rangle \langle F_i \| p^1 \| F_h\rangle}{(\omega_{eh}/2) + \epsilon_h - \epsilon_i}, \quad (21)$$

where the angular factor is given by

$$\mathcal{A}(M_e M_h; F_e F_h F_i; \mathbf{e}_\sigma) = \sum_{q_1 q_2 M_i} (-1)^{q_1+q_2+F_e-M_e+F_i-M_i} (e_\sigma)_{-q_1} (e_\sigma)_{-q_2} \times \begin{pmatrix} F_e & 1 & F_i \\ -M_e & q_2 & M_i \end{pmatrix} \begin{pmatrix} F_i & 1 & F_h \\ -M_i & q_1 & M_h \end{pmatrix}. \quad (22)$$

In Eq. (21), the sum over i is over all shells (in both the VB and the CB), with F_i the total angular momentum of the shell. In Eq. (22), M_i is the z component of the total angular momentum [see Eq. (8)], and q_1 and q_2 are the spherical components of $\mathbf{e}_\sigma$, which take the values 0, ± 1. Formulas for the reduced single-particle momentum matrix elements $\langle F_a \| p^1 \| F_b\rangle$ appearing in Eq. (21), for states of spherical form (8), were derived in our earlier work [20]. These formulas include all $\mathbf{k}\cdot\mathbf{p}$ corrections arising from the coupling of the VB and the CB and apply to both interband and intraband transitions. Expressions for the reduced matrix elements in the EMA follow from these formulas by letting the VB-CB coupling go to zero. We evaluate Eq. (21) numerically, using the HF basis set to complete the sum over intermediate states i. The substates M_e, M_h, q_1, q_2, and M_i appearing in the $3j$ symbols in Eq. (22) are also summed over numerically.

The amplitude given in Eqs. (21) and (22) depends explicitly on the polarization vector $\mathbf{e}_\sigma$, which will allow us to determine the small polarization dependence of the two-photon cross section (see Sec. III B). Two special cases are linear polarization, where we can set $(e_\sigma)_0 = 1$ and $(e_\sigma)_{\pm 1} = 0$, and circular polarization, where $(e_\sigma)_{+1} = 1$ and $(e_\sigma)_{0,-1} = 0$ is a possible choice.

2. Cubic potential

For the cubic NC, we restrict ourselves to a simpler approximation, which will enable us to to derive an analytical formula for the two-photon cross section. We shall assume the EMA, noninteracting states e and h, and we also suppose that the NC has an infinite potential barrier at the surface, as in Eqs. (3)–(5). An immediate consequence of these approximations (for any symmetry of the confining potential) is that the envelope wave functions (4) are independent of the band effective mass m_λ^*. Thus, for any electron state c in the CB, there is an "image" *hole* state, which we denote $\bar{c}$, in the VB with an identical envelope wave function to c (if we choose the phase conventions to be the same). Similarly, each hole state v in the VB has an image *electron* state $\bar{v}$ in the CB.

In the EMA, the wave function factorizes into a product of an envelope function and a Bloch function, and an interband matrix element between a CB state c and a VB state v then involves a simple overlap of envelope functions [31],

$$\langle c|\mathbf{e}_\sigma\cdot\mathbf{p}|v\rangle = \langle c|v\rangle_{\text{env}} \langle c|\mathbf{e}_\sigma\cdot\mathbf{p}|v\rangle_B, \quad (23)$$

where the subscripts "env" and B denote matrix elements over the envelope function and Bloch parts of the wave function, respectively. Similarly, an intraband matrix element satisfies

$$\langle c|\mathbf{e}_\sigma\cdot\mathbf{p}|c'\rangle = \frac{1}{m_e^*}\langle c|\mathbf{e}_\sigma\cdot\mathbf{p}|c'\rangle_{\text{env}}\langle c|c'\rangle_B, \quad (24)$$

$$\langle v|\mathbf{e}_\sigma\cdot\mathbf{p}|v'\rangle = -\frac{1}{m_h^*}\langle v|\mathbf{e}_\sigma\cdot\mathbf{p}|v'\rangle_{\text{env}}\langle v|v'\rangle_B. \quad (25)$$

The effective-mass factors $1/m_e^*$ and $1/m_h^*$ here result from higher-order $\mathbf{k}\cdot\mathbf{p}$ corrections [31]. The minus sign in Eq. (25) arises because we adopt the convention that all states (and energy eigenvalues) are written as if they refer to electronic states, whether they lie in the VB or the CB. The electron m_e^* and hole m_h^* effective masses are defined to be positive.

In the EMA, the degeneracy of the states c and v can be described by two indices, a Bloch magnetic substate μ_i and an envelope-function "substate" m_i (where $i = c$ or v). The indices μ_c and μ_v have the values $\pm\frac{1}{2}$. For a cubic confining potential, m_i enumerates the degenerate permutations of n_x, n_y, and n_z in Eqs. (4) and (5). From orthonormality, we have

$$\langle c|v\rangle_{\text{env}} = \delta(c, \bar{v})\delta(m_c, m_v), \quad (26)$$

$$\langle c|c'\rangle_B = \delta(\mu_c, \mu_{c'}), \quad \langle v|v'\rangle_B = \delta(\mu_v, \mu_{v'}). \quad (27)$$

It follows from Eq. (26) that only one intermediate state contributes to each of the two-photon amplitudes $\mathcal{M}_{eh}^{(a)}$ and $\mathcal{M}_{eh}^{(b)}$ [Eqs. (12) and (13)]. These are $r = \bar{h}$ for $\mathcal{M}_{eh}^{(a)}$ and $a = \bar{e}$ for $\mathcal{M}_{eh}^{(b)}$. Hence, using Eqs. (24)–(27), we find

$$\mathcal{M}_{eh}^{(a)} = \frac{1}{m_e^*}\frac{\langle e m_e|\mathbf{e}_\sigma\cdot\mathbf{p}|\bar{h}m_h\rangle_{\text{env}}\langle\bar{h}\mu_e|\mathbf{e}_\sigma\cdot\mathbf{p}|h\mu_h\rangle_B}{(\omega_{eh}/2)+\epsilon_h-\epsilon_{\bar{h}}}, \quad (28)$$

$$\mathcal{M}_{eh}^{(b)} = \frac{1}{m_h^*}\frac{\langle e\mu_e|\mathbf{e}_\sigma\cdot\mathbf{p}|\bar{e}\mu_h\rangle_B\langle\bar{e}m_e|\mathbf{e}_\sigma\cdot\mathbf{p}|hm_h\rangle_{\text{env}}}{(\omega_{eh}/2)+\epsilon_{\bar{e}}-\epsilon_e}, \quad (29)$$

when the laser is on resonance $2\omega = \omega_{eh}$. Because e and $\bar{e}$ (and h and $\bar{h}$) have identical envelope wave functions, the product of matrix elements on the numerator of Eq. (28) equals that in Eq. (29).

To sum the amplitude squared over degenerate final states (16), we note that

$$\sum_{\mu_e\mu_h}|\langle\bar{h}\mu_e|\mathbf{e}_\sigma\cdot\mathbf{p}|h\mu_h\rangle_B|^2 = \frac{1}{3}(\mathbf{e}_\sigma^*\cdot\mathbf{e}_\sigma)|\langle J_{\text{CB}}\|p^1\|J_{\text{VB}}\rangle|^2 = \frac{1}{3}E_P, \quad (30)$$

where we have used $\mathbf{e}_\sigma^*\cdot\mathbf{e}_\sigma = 1$ from the normalization of the polarization vector, and $|\langle J_{\text{CB}}\|p^1\|J_{\text{VB}}\rangle|^2 = E_P$, which can be taken as the definition of the Kane parameter. Similarly, we have

$$\sum_{m_e m_h}|\langle e m_e|\mathbf{e}_\sigma\cdot\mathbf{p}|\bar{h}m_h\rangle_{\text{env}}|^2 = \sum_{m_e m_h}|\langle e m_e|p_z|\bar{h}m_h\rangle_{\text{env}}|^2, \quad (31)$$

TABLE I. Material parameters for $CsPbBr_3$ used in this paper. $E_P^{(4\times4)}$ and $E_P^{(8\times8)}$ are estimates of the Kane parameter deduced from the 4×4 and $8\times8\,\mathbf{k}\cdot\mathbf{p}$ models [20]. See Sec. III A for further explanation.

	$CsPbBr_3$
μ^* (m_0)	0.126[a]
$m_e^* = m_h^*$ (m_0)	0.252
E_g (eV)	2.342[a]
$E_P^{(4\times4)}$ (eV)	27.9[b]
$E_P^{(8\times8)}$ (eV)	16.4[b]
$\varepsilon_{\rm eff}$	7.3[a]
$\varepsilon_{\rm opt}$	4.9[c]
$\varepsilon_{\rm out}$	2.4[d]

[a]Reference [32].
[b]Reference [20].
[c]Reference [33], for a wavelength of 800 nm.
[d]Applies to toluene.

using the property

$$\sum_{m_e m_h} \langle em_e|p_i|\bar{h}m_h\rangle^*_{\rm env}\langle em_e|p_j|\bar{h}m_h\rangle_{\rm env} = 0 \quad \text{if } i\neq j, \tag{32}$$

which holds for cubic (or spherical) symmetry. The total amplitude squared now follows from Eqs. (28)–(31) to be

$$|\bar{\mathcal{M}}_{eh}|^2 = \frac{1}{3}\frac{E_P}{\Omega_{eh}^2}\sum_{m_e m_h}|\langle em_e|p_z|\bar{h}m_h\rangle_{\rm env}|^2, \tag{33}$$

where

$$\frac{1}{\Omega_{eh}} = \frac{1/m_e^*}{(\omega_{eh}/2)+\epsilon_h-\epsilon_{\bar{h}}} + \frac{1/m_h^*}{(\omega_{eh}/2)+\epsilon_{\bar{e}}-\epsilon_e}. \tag{34}$$

The amplitude squared (33) can be inserted into Eqs. (15) and (19) to find the transition rate and cross section.

The matrix element of p_z appearing in Eq. (33), for cubic wave functions (4), is given by

$$\langle n_x' n_y' n_z'|p_z|n_x n_y n_z\rangle = \delta(n_x,n_x')\delta(n_y,n_y')\delta^{\rm odd}(n_z,n_z') \times\frac{4i}{L}\frac{n_z n_z'}{n_z^2-(n_z')^2}, \tag{35}$$

where $\delta^{\rm odd}(n_z,n_z')=1$ if n_z-n_z' is an odd integer, and $\delta^{\rm odd}(n_z,n_z')=0$ otherwise. The sum over substates m_e and m_h in Eq. (33) in this case amounts to a weight factor obtained by considering the number of degenerate permutations of n_x, n_y, and n_z for any given matrix element.

Note that, within the approximations of this section, the dependence of the amplitude squared (33) (and hence the two-photon cross section) on the polarization vector $\mathbf{e}_\sigma$ has disappeared. As discussed in Sec. III B, the small polarization dependence of the two-photon cross section arises instead from higher-order effects, such as $\mathbf{k}\cdot\mathbf{p}$ corrections.

III. APPLICATION TO INORGANIC PEROVSKITES

A. Material parameters

The material parameters for $CsPbBr_3$ assumed in the calculations are given in Table I. The reduced effective mass $\mu^* = m_e^* m_h^*/(m_e^*+m_h^*)$ and the band gap E_g are taken from the cryogenic measurements of Yang *et al.* [32]. The individual electron and hole effective masses are not known, but experimental [34] and theoretical [1,25,35] evidence suggests that they are approximately equal in inorganic perovskites, so we shall assume $m_e^* = m_h^*$.

The Kane parameter E_P has not been measured directly in $CsPbBr_3$. In Ref. [20], we estimated E_P from the $4\times4\,\mathbf{k}\cdot\mathbf{p}$ model for the s-like VB and the $p_{1/2}$-like CB, and from an $8\times8\,\mathbf{k}\cdot\mathbf{p}$ model including also the higher-lying $p_{3/2}$-like CB, by assuming that remote bands made a negligible contribution to the effective masses. The resulting estimates of E_P are given in Table I. We take the view that E_P is uncertain at present, a conservative range being $10\text{ eV}\leqslant E_P\leqslant 32\text{ eV}$. In most of the calculations in the next section, we will use the illustrative value $E_P = 20$ eV, which is intermediate between the values given by the 4×4 and $8\times8\,\mathbf{k}\cdot\mathbf{p}$ models.

The "effective" dielectric constant $\varepsilon_{\rm eff}$ in Table I was inferred by Yang *et al.* [32] from a measurement of the binding energy of the bulk exciton. We use $\varepsilon_{\rm in}=\varepsilon_{\rm eff}$ to screen the Coulomb interactions in the HF procedure [see Eq. (2)] because the length scale for $\varepsilon_{\rm eff}$ is of order the Bohr radius a_B, which is comparable to the size of the NCs that we will consider ($2a_B = 6.1$ nm for the parameters in Table I). We also need the optical dielectric constant $\varepsilon_{\rm in}'=\varepsilon_{\rm opt}$ to calculate the dielectric screening factor f_ε [Eq. (10)]. We take the value from Ref. [33] for a wavelength $\lambda = 800$ nm, which is used for the principal measurements discussed in the next section. Note that $\varepsilon_{\rm eff}$ and $\varepsilon_{\rm opt}$ differ significantly for $CsPbBr_3$, an indication that the dielectric function varies rapidly with frequency and length scale.

B. Theoretical two-photon cross section

In this work, we consider two-photon absorption from the highest-lying VB (s-like, R_6^+) to the lowest-lying CB ($p_{1/2}$-like, R_6^-) around the R point of the Brillouin zone, and neglect transitions to higher-lying bands. In particular, we neglect the transition $R_6^+\to R_8^-$ to the spin-orbit split-off $p_{3/2}$-like CB (R_8^-), which lies about 1 eV above the $p_{1/2}$-like band at the R point [25,36]. A steplike feature is often seen in one-photon absorption spectra of NCs of $CsPbBr_3$ (e.g., see Refs. [13,37]) lying about 1 eV above threshold at an energy of 3.0–3.2 eV (for an edge length $L\approx 9$ nm), which is likely to be due to the onset of the $R_6^+\to R_8^-$ transition [20]. Therefore, the range of validity of the present calculations extends from the threshold, at a total energy of about 2.3 eV, up to a total energy of about 3.1 eV.

In Fig. 2, we show two-photon transition strengths $T_{eh}^{(2)}$ calculated in various approximations. Here, $T_{eh}^{(2)}$ is defined as the coefficient of the line-shape function $\Delta_{eh}(\omega-\omega_{eh}/2)$ in the total cross section (19),

$$T_{eh}^{(2)} = \frac{32\pi^3}{n_{\rm out}^2 c^2\omega_{eh}^2} f_\varepsilon^4 |\bar{\mathcal{M}}_{eh}|^2, \tag{36}$$

where we have assumed the laser to be on resonance, $\omega=\omega_{eh}/2$, for the transition to a final-state exciton (e,h). The top two panels in Fig. 2 both assume the EMA and noninteracting states e and h. One sees that the detailed transition strengths for a cubic NC (top-right panel) differ significantly from those

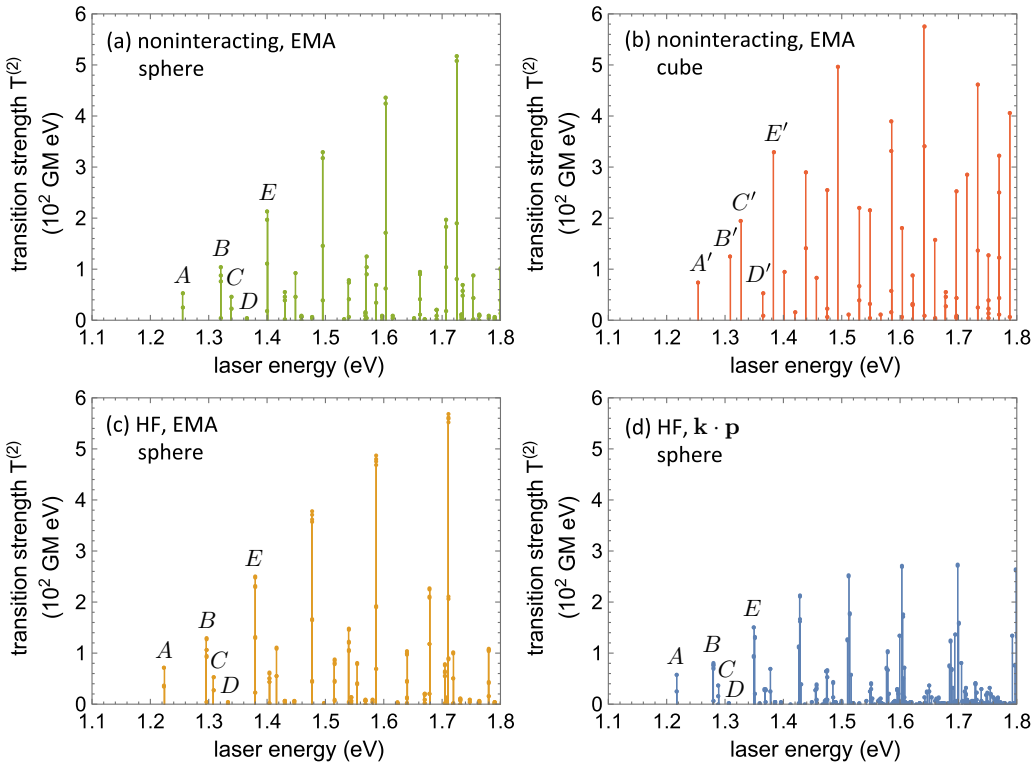

FIG. 2. Two-photon transition strengths $T^{(2)}_{eh}$ [Eq. (36)] in various approximations for final-state excitons (e, h). The NC has edge length $L = 9$ nm and the Kane parameter is taken to be $E_P = 20$ eV. The position of the lines indicates the resonant energy $\omega = \omega_{eh}/2$ of the laser required to excite the exciton, where ω_{eh} is the exciton energy. Notation: EMA, effective-mass approximation; HF, Hartree-Fock approximation; $\mathbf{k}\cdot\mathbf{p}$, the 4×4 $\mathbf{k}\cdot\mathbf{p}$ approximation. (a) Shows transition strengths within the EMA assuming the final-state electron and hole to be noninteracting, and uses the quasicubic spherical confining potential. (b) Similar to (a), but the confining potential is a perfect cube. In (c), we use the EMA and the quasicubic spherical confining potential, and treat the (e, h) exciton in the HF approximation. (d) Similar to (c), but the 4×4 $\mathbf{k}\cdot\mathbf{p}$ approximation is used instead of the EMA. We indicate the quantum numbers of the first few exciton final states by A, B, . . ., and A', B', . . ., etc. For the spherical potential: A indicates $1S_e$-$1P_h$ or $1S_h$-$1P_e$, which are degenerate for VB-CB symmetry (as assumed here); we denote these states collectively by $1S$-$1P$. Similarly, B indicates $1P$-$1D$, C indicates $2S$-$1P$, D indicates $1S$-$2P$, and E indicates $1D$-$1F$. For the cubic potential: the states e or h are denoted by three integers (n_x, n_y, n_z) [see Eq. (4)]. A' indicates $(1, 1, 1)_e$-$(1, 1, 2)_h$ or $(1, 1, 1)_h$-$(1, 1, 2)_e$, which are degenerate for VB-CB symmetry, together with the degenerate permutations of n_x, n_y, and n_z; we denote all these states collectively by (1, 1, 1)-(1, 1, 2). Similarly, B' indicates (2, 1, 1)-(2, 1, 2); C' indicates (1, 1, 2)-(1, 1, 3); D' indicates (2, 2, 1)-(2, 2, 2) and (1, 1, 1)-(1, 1, 4), which are degenerate for VB-CB symmetry; and E' indicates (2, 1, 2)-(2, 1, 3).

for the quasicubic spherical potential (top-left panel). As we will see below, however, the broadened cross sections given by the two sets of transition strengths are in fact quite similar.

The two lower panels in Fig. 2 assume the HF approximation for the final-state exciton (e, h). In this case, we also adjust the exciton energy ω_{eh} to correspond to the HF energy for the state [21]

$$\omega_{eh} = \epsilon_e - \epsilon_h - E^{\text{Coul}}_{eh}. \tag{37}$$

We make the further approximation that the Coulomb energy E^{Coul}_{eh} is approximately constant, independent of (e, h), and can be set equal to the Coulomb energy for the ground-state $1S_e$-$1S_h$ exciton $E^{\text{Coul}}_{eh} = E^{\text{Coul}}_{1S}$. The two panels on the left of Fig. 2 allow one to assess the effect of using the HF approximation for the exciton (e, h) instead of assuming noninteracting particles. At HF level, the transitions are shifted to a slightly smaller energy and increased slightly in strength, but overall the two sets of transition strengths are quite similar.

The role of $\mathbf{k}\cdot\mathbf{p}$ corrections can be seen by comparing the two sets of transition strengths in the lower panels of Fig. 2. The most striking effect of the $\mathbf{k}\cdot\mathbf{p}$ corrections is to decrease the overall transition strength for corresponding transitions by up to a factor of about 2, especially for the higher-energy transitions. This can be traced to reductions of both the intraband and interband transition matrix elements in the numerators of Eqs. (12) and (13), when $\mathbf{k}\cdot\mathbf{p}$ corrections are included. (The $\mathbf{k}\cdot\mathbf{p}$ corrections to interband matrix elements were previously discussed in Ref. [20].) The $\mathbf{k}\cdot\mathbf{p}$ approach can also be seen to lead to an increase in the number of final-state excitons per unit energy (reduction in the energy spacing of the dominant transitions) and to give numerous new transitions with weak transition strength. For instance, a final-state exciton $(1S_{1/2})_e$-$(1F_{5/2})_h$ is forbidden by angular-momentum selection rules in the EMA because there is no possible intermediate state i in Eq. (14). However, the same transition is allowed in the $\mathbf{k}\cdot\mathbf{p}$ approximation with intermediate states $(nD_{3/2})_h$ or $(n'P_{3/2})_e$ by virtue of the small components ($\mathbf{k}\cdot\mathbf{p}$ admixtures) of the states (8), as can be seen by inspecting the selection rules in the formula for the reduced matrix element $\langle F_a \| p^1 \| F_b \rangle$ given in Ref. [20]. In addition, the

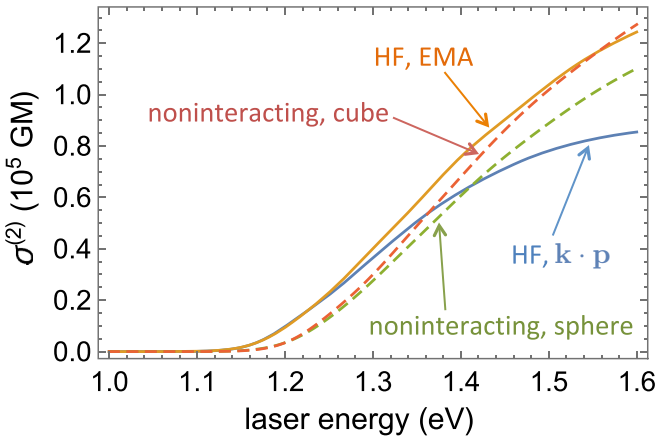

FIG. 3. Broadened two-photon cross sections $\sigma^{(2)}(\omega)$ [Eq. (20)] in various approximations, derived from the transition strengths in Figs. 2(a)–2((d). The NC has edge length $L = 9$ nm and the Kane parameter is taken to be $E_P = 20$ eV. Dashed lines: noninteracting EMA approximation, for quasicubic spherical confining potential or cubic potential [corresponding to Figs. 2(a) and 2(b), respectively]. Solid lines: Hartree-Fock approximation for quasicubic spherical potential, within the EMA or the 4×4 $\mathbf{k} \cdot \mathbf{p}$ model [corresponding to Figs. 2(c) and 2(d), respectively].

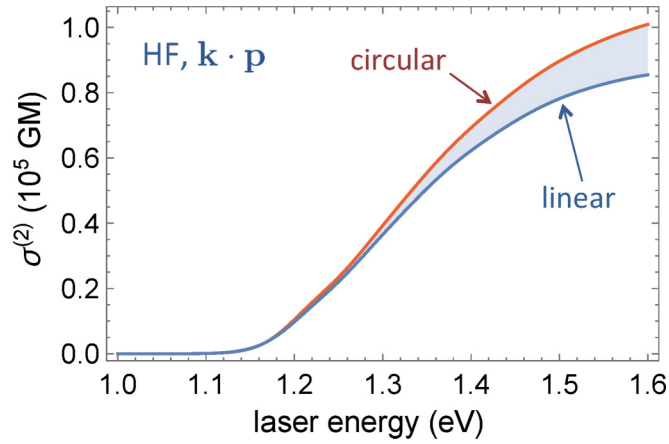

FIG. 4. Polarization dependence of the two-photon cross section $\sigma^{(2)}(\omega)$ [Eq. (20)] as a function of laser energy ω for a NC of edge length $L = 9$ nm (and $E_P = 20$ eV), within the Hartree-Fock and 4×4 $\mathbf{k} \cdot \mathbf{p}$ approximations. The upper curve is for circular polarization, the lower curve for linear polarization; the shaded region is for elliptical polarizations.

transition strengths in Fig. 2 reveal the small "fine-structure" splittings (e.g., of $P_{1/2}$ and $P_{3/2}$ states) induced by the $\mathbf{k} \cdot \mathbf{p}$ coupling (more visible for the higher-energy transitions).

Figure 3 shows the two-photon cross sections (20) derived from the transition strengths in Fig. 2, after broadening the transitions. For this purpose, as in our earlier work on one-photon absorption [20], we choose a Gaussian line-shape function emphasizing inhomogeneous line-broadening mechanisms

$$\Delta_{eh}(\omega - \omega_{eh}/2) = \frac{1}{\sigma_{eh}\sqrt{\pi/2}} \exp\left[-\frac{(2\omega - \omega_{eh})^2}{2\sigma_{eh}^2}\right]. \quad (38)$$

The width parameters σ_{eh} here are defined and calculated in the same way as was done for one-photon absorption in Ref. [20]:

$$\sigma_{eh}^2 = \left(\sigma_{eh}^{\text{size}}\right)^2 + (\sigma^{\text{other}})^2. \quad (39)$$

The width contribution $\sigma_{eh}^{\text{size}}$ is due to the distribution of NC sizes in the ensemble, and is calculated assuming a range of edge lengths $\delta L/L = 8\%$, while σ^{other} is a constant width, here chosen to be $\sigma^{\text{other}} = 80$ meV, which takes account phenomenologically of other broadening mechanisms (distribution of NC shape deformations, phonons, etc.) We used similar values of the parameters for one-photon absorption spectra in Ref. [20]. The cross sections near $2\omega = 3.1$ eV (discussed in the comparison with experiment in the next section) are rather insensitive to variations in these width parameters. For σ^{other} in the range 50 to 100 meV and for $\delta L/L$ in the range 5% to 10% (typical of experiments), one finds a variation of only about $\pm 5\%$ in the cross section for $2\omega = 3.1$ eV.

The dashed curves in Fig. 3 correspond to the top panels in Fig. 2. We see that, although the detailed transitions are different for the cubic and spherical (quasicubic) confining potentials, the average transition strength of the two is similar, in the sense that they lead to similar broadened two-photon cross sections. The two cross sections are very close near the threshold [as is to be expected, because the quasicubic radius R, Eq. (7), was fitted to the ground-state energy in the cube], but the difference between them grows slowly as the energy increases, reaching about 15% at the maximum energy considered here ($2\omega = 3.1$ eV). The performance of the quasicubic potential for one-photon absorption is similar [20]; for the same broadening parameters, the cubic cross section is about 17% larger than the quasicubic one for a one-photon absorption energy of 3.1 eV.

We also see from Fig. 3 that the overall effect of the $\mathbf{k} \cdot \mathbf{p}$ corrections on the cross section is rather large. The reduction in transition strength observed in Fig. 2 is partially offset by the increased number of states per unit energy and the extra strength of the new transitions, so that, for $2\omega = 3.1$ eV, the $\mathbf{k} \cdot \mathbf{p}$ cross section is about 30% smaller than the EMA cross section.

We showed in Sec. II B 2 that $\sigma^{(2)}(\omega)$ is independent of the polarization $\mathbf{e}_\sigma$ if one assumes noninteracting particles and the EMA (and an infinite barrier at the NC surface). The key point in the derivation was that, within these approximations, the set of envelope functions for an electron is identical to that for a hole. Because here we assume $m_e^* = m_h^*$, the equality of the two sets of envelope functions holds also at HF level in the EMA, and $\sigma^{(2)}(\omega)$ is then also independent of $\mathbf{e}_\sigma$. (This result would not hold in general for $m_e^* \neq m_h^*$.) Therefore, to estimate the polarization dependence of $\sigma^{(2)}$, we need to consider the $\mathbf{k} \cdot \mathbf{p}$ corrections, using the formalism of Sec. II B 1. The result is shown in Fig. 4. The polarization dependence of $\sigma^{(2)}$ is generally small, but increases with increasing energy, reaching a discrepancy of about 16% between circular and linear polarization at $2\omega = 3.1$ eV.

C. Comparison with experiment

We now turn to a comparison with the available experimental data. Chen *et al.* [13] made a careful study of the

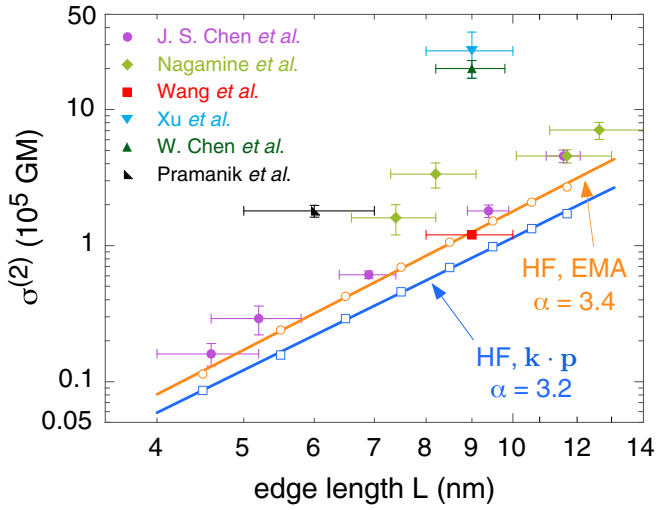

FIG. 5. Log-log plot of the two-photon absorption cross section $\sigma^{(2)}(\omega)$ [Eq. (20)] at a total energy $2\omega = 3.1$ eV ($\lambda = 800$ nm) vs edge length L. Unfilled circles and squares: theoretical cross sections (assuming $E_P = 20$ eV) calculated within the Hartree-Fock approximation (HF) and either the effective-mass approximation (EMA) or the $4 \times 4\,\mathbf{k}\cdot\mathbf{p}$ approximation ($\mathbf{k}\cdot\mathbf{p}$). Straight lines: fits of the theoretical cross section through the calculated points, assuming a power-law dependence, $\sigma^{(2)}(\omega) \propto L^{\alpha}$, with the exponent α given by the slope of the straight-line fit in logarithmic space. Filled circles/diamonds/squares/triangles: experimental points. Wang *et al.*, Ref. [10]; Xu *et al.*, Ref. [12]; J. S. Chen *et al.*, Ref. [13]; W. Chen *et al.*, Ref. [15]; Nagamine *et al.*, Ref. [14]; Pramanik *et al.*, Ref. [16].

two-photon cross section at a total energy $2\omega = 3.1$ eV ($\lambda = 800$ nm) as a function of NC size, for edge lengths from $L = 4.6$ to 11.4 nm, finding a power-law dependence on L. Theoretical cross sections at the same energy and over the same size range are shown Fig. 5. The linearity of the log-log plot confirms that the theoretical data fit well a power-law dependence $\sigma^{(2)}(\omega) \propto L^{\alpha}$, with a theoretical exponent $\alpha = 3.4$ in the EMA and $\alpha = 3.2$ in the $\mathbf{k}\cdot\mathbf{p}$ model. These exponents are in excellent agreement with the experimental value $\alpha_{\text{expt}} = 3.3 \pm 0.2$ [13].

Several terms contributing to $\sigma^{(2)}(\omega)$ are strongly L dependent. It can be seen from the approximate expression (33) that the amplitude squared $|\bar{\mathcal{M}}_{eh}|^2$ is proportional to an intraband matrix element squared $|\langle e m_e | p_z | \bar{h} m_h \rangle_{\text{env}}|^2$ and to an energy parameter $1/\Omega_{eh}^2$. A detailed analysis shows that the L dependence of the matrix element, which is given by Eq. (35), is approximately canceled by the L dependence of the energy parameter (for a fixed observation energy $\omega \approx \omega_{eh}$, and over the size range $L = 4.6$ to 11.4 nm). The dominant L-dependent term in the two-photon cross section is then the number of final-state excitons per unit energy, which is associated with the sum over (e, h) in Eq. (19). Now, in 3D the number of states per unit energy is proportional to the volume of the confining box, at least, in the limit of large box sizes [29]. For the NC sizes considered here, the spectra are quite discrete at energies of $2\omega = 3.1$ eV (see Fig. 2), but the broadening of the spectral lines leads to an average density of states at the observation energy, which retains an approximate L^3 dependence. A similar effect is observed for the one-photon absorption cross section, where the exponent is also close to three [13,20].

The experimental data for absolute (normalized) two-photon cross sections at a total energy $2\omega = 3.1$ eV [10,12–16] are summarized in Fig. 5. One sees that there is a large spread in the experimental values, which in some cases differ by one to two orders of magnitude for a given edge length L. This perhaps reflects the difficulties in the various procedures that have been used to normalize the experimental cross sections. Our theoretical results are in fair agreement with the group of measurements at the lower end of the range of values.

The main uncertainties in our theoretical two-photon cross sections are due to the following:

(i) *Correlation*. We have not included correlation (many-body effects beyond HF) in the present calculations. Correlation corrections to one-photon absorption can be large in intermediate or weak confinement [38] and are known to enhance the one-photon transition rate at threshold in NCs of $CsPbBr_3$ by factors as large as 4–6 [20,25]. However, a perturbative study of one-photon absorption in Ref. [20], based on calculations of the electron-photon vertex correction, showed that the enhancement factor approached unity rapidly as the energy increased, reaching a value of around only 1.4 for a total energy of 3.1 eV. We believe that a similar effect holds for two-photon absorption.

To see this, we note first that a single intermediate state dominates the sum over states in the two-photon amplitudes (12) and (13), specifically, $r = \bar{h}$ for $\mathcal{M}_{eh}^{(a)}$ and $a = \bar{e}$ for $\mathcal{M}_{eh}^{(b)}$, in the notation of Sec. II B 2. This result holds exactly in the EMA used in Sec. II B 2, but is approximately true also when $\mathbf{k}\cdot\mathbf{p}$ corrections are included, because in that case there is still an approximate orthonormality between electron and hole envelope functions. Hence, we can rewrite Eqs. (12) and (13) approximately as

$$\mathcal{M}_{eh}^{(a)} \approx \frac{\langle e|\mathbf{e}_\sigma\cdot\mathbf{p}|\bar{h}\rangle_{\text{intra}}\langle\bar{h}|\mathbf{e}_\sigma\cdot\mathbf{p}|h\rangle_{\text{inter}}}{(\omega_{eh}/2) + \epsilon_h - \epsilon_{\bar{h}}}, \tag{40}$$

$$\mathcal{M}_{eh}^{(b)} \approx -\frac{\langle e|\mathbf{e}_\sigma\cdot\mathbf{p}|\bar{e}\rangle_{\text{inter}}\langle\bar{e}|\mathbf{e}_\sigma\cdot\mathbf{p}|h\rangle_{\text{intra}}}{(\omega_{eh}/2) + \epsilon_{\bar{e}} - \epsilon_e}. \tag{41}$$

Here, the states e, h, etc., represent the full state, including both envelope functions and Bloch states, and the laser is assumed to be on resonance for the transition to (e, h), so that $2\omega = \omega_{eh}$. We have indicated explicitly the intraband or interband nature of each matrix element.

Now, the potentially large enhancement factors that occur for one-photon absorption are associated with the *interband* matrix elements in Eqs. (40) and (41). The intraband matrix elements and the energy factors may be expected to have correlation corrections typical of atoms and molecules, thus up to several tens of a percent [39,40]. (For example, correlation corrections to energies in NCs of $CsPbBr_3$ were calculated in Ref. [21].) One observes that, for a total energy $2\omega = \omega_{eh} = 3.1$ eV, the two-photon amplitudes (40) and (41) involve the same interband matrix elements $\langle\bar{h}|\mathbf{e}_\sigma\cdot\mathbf{p}|h\rangle_{\text{inter}}$ and $\langle e|\mathbf{e}_\sigma\cdot\mathbf{p}|\bar{e}\rangle_{\text{inter}}$ that would contribute to one-photon absorption at approximately the same total energy. Therefore, it is reasonable to expect that the enhancement factor of the two-photon transition rate due to correlation is similar, namely,

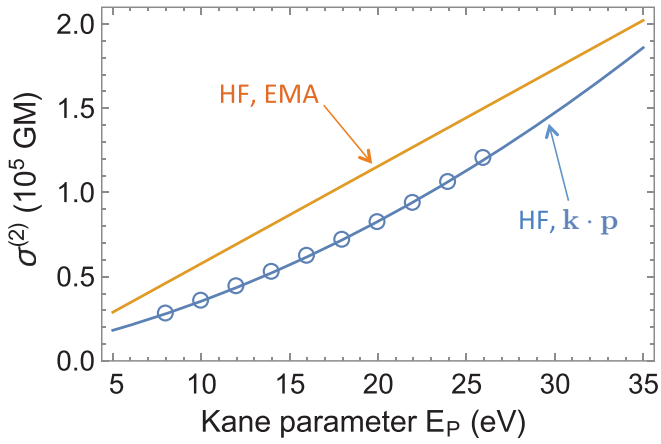

FIG. 6. Two-photon cross section $\sigma^{(2)}(\omega)$ [Eq. (20)] at a total energy $2\omega = 3.1$ eV ($\lambda = 800$ nm) vs the Kane parameter E_P for a NC of edge length $L = 9$ nm, using the Hartree-Fock (HF) approximation. Upper line: effective-mass approximation (EMA), which gives an exactly linear relationship. Lower line: 4×4 $\mathbf{k} \cdot \mathbf{p}$ approximation; the curved line is a quadratic fit through the calculated points indicated by circles.

around 1.4 (with further corrections from correlation in the intraband matrix elements and the energy denominator).

(ii) *Value of the Kane parameter* E_P. We assumed $E_P = 20$ eV for the calculations in Fig. 5, a value that is intermediate between the estimated values from the 4×4 and 8×8 $\mathbf{k} \cdot \mathbf{p}$ models (see Table I). Now, the two-photon cross section is approximately proportional to E_P, as shown in Fig. 6. From Eq. (33), it follows that this proportionality is exact in the EMA. In the $\mathbf{k} \cdot \mathbf{p}$ model, however, the coupling of the VB and CB is also controlled by E_P, and this introduces nonlinear terms, which are apparent in Fig. 6. Note that the 4×4 $\mathbf{k} \cdot \mathbf{p}$ model used here is free of spurious intragap states (which are observed in $\mathbf{k} \cdot \mathbf{p}$ models applied to NCs of certain III-V and II-VI semiconductors [41]) provided $E_P \lesssim 28$ eV. If we assume an uncertainty of $\pm 50\%$ in the value of E_P, the two-photon cross section would be uncertain by roughly the same amount.

Other, smaller sources of theoretical uncertainty arise from the use of the quasicubic spherical potential (as discussed in Secs. II B and III B), and from the possible onset of the $R_6^+ \to R_8^-$ transition to the $p_{3/2}$-like CB [20] at the higher energies. After taking all these theoretical uncertainties into account, however, the present calculations of $\sigma^{(2)}(\omega)$ still strongly favor the group of measurements in Fig. 5 at the lower end of the range of values.

IV. CONCLUSIONS

We have presented calculations of the two-photon absorption cross section $\sigma^{(2)}(\omega)$ of NCs of $CsPbBr_3$ at various levels of theory. The band structure was described by a 4×4 $\mathbf{k} \cdot \mathbf{p}$ model or within the EMA, and excitons were treated by a HF approximation or as noninteracting confined particles. Calculations were made from the threshold for two-photon absorption up to a total energy $2\omega = 3.1$ eV, and were restricted to the lowest-energy band transition $R_6^+ \to R_6^-$.

The $\mathbf{k} \cdot \mathbf{p}$ corrections to $\sigma^{(2)}(\omega)$ were found to be rather large, leading to an overall reduction of about 30% in $\sigma^{(2)}(\omega)$ at the highest energy considered ($2\omega = 3.1$ eV). We found that cubic NCs could be quite well represented by a "quasicubic" spherical confining potential, which was fitted to the ground-state energies of the cube; the error in $\sigma^{(2)}(\omega)$ due to the quasicubic potential rose with increasing photon energy ω from zero near threshold to a maximum error of about 15% at $2\omega = 3.1$ eV. The two-photon cross section was shown analytically to be independent of polarization in the EMA, but to acquire a small polarization dependence when $\mathbf{k} \cdot \mathbf{p}$ corrections were considered. The difference in the cross section between linear and circular polarization reached a maximum of about 16% at $2\omega = 3.1$ eV.

The calculations reproduce very well a power-law dependence on NC size, $\sigma^{(2)}(\omega) \propto L^{\alpha}$, as was observed experimentally by Chen *et al.* [13], with theoretical exponents $\alpha = 3.4$ (EMA) and $\alpha = 3.2$ (4×4 $\mathbf{k} \cdot \mathbf{p}$ model) in excellent agreement with the experimental result $\alpha_{\text{expt}} = 3.3 \pm 0.2$ [13]. The dominant term contributing to this exponent was shown to be the number of final-state excitons per unit energy. Measured values of the absolute (normalized) cross section $\sigma^{(2)}(\omega)$ [10,12–16] contain significant discrepancies, with reported values differing by as much as a factor of 25 for certain NC sizes. Our calculations provide strong theoretical evidence in favor of a group of measurements at the lower end of the range of reported values of $\sigma^{(2)}(\omega)$.

The calculations reported here can be improved upon in various ways in future work. A leading uncertainty arose from the value of the Kane parameter E_P for $CsPbBr_3$. We used an estimated value $E_P \approx 20$ eV derived by considering 4×4 and 8×8 $\mathbf{k} \cdot \mathbf{p}$ models of the band structure [20]. It would be useful to carry out further studies with *ab initio* atomistic approaches. Calculations within density-functional theory [1,25] gave a value of E_P of around 40 eV, which seems too high. It might be possible to make further progress by, for example, using relativistic *GW* methods, or by including phonon-mediated effects. Also interesting would be to consider explicitly the correlation corrections to the two-photon cross section, for example, by generalizing the vertex-correction methods used for the one-photon cross section $\sigma^{(1)}(\omega)$ in Ref. [20], although such many-body approaches would be significantly more complicated for two-photon processes.

ACKNOWLEDGMENTS

The authors would like to thank Sum T. C. for helpful discussions. They acknowledge the France-Singapore Merlion Project 2.05.16 for supporting mutual visits. T.P.T.N. and S.A.B. are grateful to F. Schuster of the CEA's PTMA program for financial support. C.G. gratefully acknowledges financial support from the National Research Foundation through the Competitive Research Program, Grant No. NRF-CRP14-2014-03.

[1] L. Protesescu, S. Yakunin, M. I. Bodnarchuk, F. Krieg, R. Caputo, C. H. Hendon, R. X. Yang, A. Walsh, and M. V. Kovalenko, Nanocrystals of cesium lead halide perovskites ($CsPbX_3$, X = Cl, Br, and I): Novel optoelectronic materials showing bright emission with wide color gamut, Nano Lett. **15**, 3692 (2015).

[2] A. Swarnkar, R. Chulliyil, V. K. Ravi, M. Irfanullah, A. Chowdhury, and A. Nag, Colloidal $CsPbBr_3$ perovskite nanocrystals: Luminescence beyond traditional quantum dots, Angew. Chem., Int. Ed. **54**, 15424 (2015).

[3] G. Rainò, G. Nedelcu, L. Protesescu, M. I. Bodnarchuk, M. V. Kovalenko, R. F. Mahrt, and T. Stöferle, Single cesium lead halide perovskite nanocrystals at low temperature: Fast single photon emission, reduced blinking, and exciton fine structure, ACS Nano **10**, 2485 (2016).

[4] F. Krieg, S. T. Ochsenbein, S. Yakunin, S. ten Brinck, P. Aellen, A. Suess, B. Clerc, D. Guggisberg, O. Nazarenko, Y. Shynkarenko, S. Kumar, C. J. Shih, I. Infante, and M. V. Kovalenko, Colloidal $CsPbX_3$ (X = Cl, Br, I) nanocrystals 2.0: Zwitterionic capping ligands for improved durability and stability, ACS Energy Lett. **3**, 641 (2018).

[5] W. Deng, X. Z. Xu, X. J. Zhang, Y. D. Zhang, X. C. Jin, L. Wang, S. T. Lee, and J. S. Jie, Organometal halide perovskite quantum dot light-emitting diodes, Adv. Funct. Mater. **26**, 4797 (2016).

[6] G. R. Li, F. W. R. Rivarola, N. J. L. K. Davis, S. Bai, T. C. Jellicoe, F. de la Pena, S. C. Hou, C. Ducati, F. Gao, R. H. Friend, N. C. Greenham, and Z. K. Tan, Highly efficient perovskite nanocrystal light-emitting diodes enabled by a universal crosslinking method, Adv. Mater. **28**, 3528 (2016).

[7] J. Pan, S. P. Sarmah, B. Murali, I. Dursun, W. Peng, M. R. Parida, J. Liu, L. Sinatra, N. Alyami, C. Zhao, E. Alarousu, T. K. Ng, B. S. Ooi, O. M. Bakr, and O. F. Mohammed, Air-stable surface-passivated perovskite quantum dots for ultra-robust, single- and two-photon-induced amplified spontaneous emission, J. Phys. Chem. Lett. **6**, 5027 (2015).

[8] S. Yakunin, L. Protesescu, F. Krieg, M. I. Bodnarchuk, G. Nedelcu, M. Humer, G. De Luca, M. Fiebig, W. Heiss, and M. V. Kovalenko, Low-threshold amplified spontaneous emission and lasing from colloidal nanocrystals of caesium lead halide perovskites, Nat. Commun. **6**, 8056 (2015).

[9] H. Utzat, W. W. Sun, A. E. K. Kaplan, F. Krieg, M. Ginterseder, B. Spokoyny, N. D. Klein, K. E. Shulenberger, C. F. Perkinson, M. V. Kovalenko, and M. G. Bawendi, Coherent single-photon emission from colloidal lead halide perovskite quantum dots, Science **363**, 1068 (2019).

[10] Y. Wang, X. M. Li, X. Zhao, L. Xiao, H. B. Zeng, and H. D. Sun, Nonlinear absorption and low-threshold multiphoton pumped stimulated emission from all-inorganic perovskite nanocrystals, Nano Lett. **16**, 448 (2016).

[11] N. S. Makarov, S. J. Guo, O. Isaienko, W. Y. Liu, I. Robel, and V. I. Klimov, Spectral and dynamical properties of single excitons, biexcitons, and trions in cesium-lead-halide perovskite quantum dots, Nano Lett. **16**, 2349 (2016).

[12] Y. Q. Xu, Q. Chen, C. F. Zhang, R. Wang, H. Wu, X. Y. Zhang, G. C. Xing, W. W. Yu, X. Y. Wang, Y. Zhang, and M. Xiao, Two-photon-pumped perovskite semiconductor nanocrystal lasers, J. Am. Chem. Soc. **138**, 3761 (2016).

[13] J. S. Chen, K. Zidek, P. Chabera, D. Z. Liu, P. F. Cheng, L. Nuuttila, M. J. Al-Marri, H. Lehtivuori, M. E. Messing, K. L. Han, K. B. Zheng, and T. Pullerits, Size- and wavelength-dependent two-photon absorption cross-section of $CsPbBr_3$ perovskite quantum dots, J. Phys. Chem. Lett. **8**, 2316 (2017).

[14] G. Nagamine, J. O. Rocha, L. G. Bonato, A. F. Nogueira, Z. Zaharieva, A. A. R. Watt, C. H. D. Cruz, and L. A. Padilha, Two-photon absorption and two-photon-induced gain in perovskite quantum dots, J. Phys. Chem. Lett. **9**, 3478 (2018).

[15] W. Chen, S. Bhaumik, S. A. Veldhuis, G. Xing, Q. Xu, M. Gratzel, S. Mhaisalkar, N. Mathews, and T. C. Sum, Giant five-photon absorption from multidimensional core-shell halide perovskite colloidal nanocrystals, Nat. Commun. **8**, 15198 (2017).

[16] A. Pramanik, K. Gates, Y. Gao, S. Begum, and P. C. Ray, Several orders-of-magnitude enhancement of multiphoton absorption property for $CsPbX_3$ perovskite quantum dots by manipulating halide stoichiometry, J. Phys. Chem. C **123**, 5150 (2019).

[17] J. Szeremeta, M. A. Antoniak, D. Wawrzyńczyk, M. Nyk, and M. Samoć, The two-photon absorption cross-section studies of $CsPbX_3$ (X = I, Br, Cl) nanocrystals, Nanomaterials **10**, 1054 (2020).

[18] K. Y. Zhang, Q. Yu, H. J. Wei, S. J. Liu, Q. Zhao, and W. Huang, Long-lived emissive probes for time-resolved photoluminescence bioimaging and biosensing, Chem. Rev. **118**, 1770 (2018).

[19] A. Ferrando, J. P. M. Pastor, and I. Suarez, Toward metal halide perovskite nonlinear photonics, J. Phys. Chem. Lett. **9**, 5612 (2018).

[20] T. P. T. Nguyen, S. A. Blundell, and C. Guet, One-photon absorption by inorganic perovskite nanocrystals: A theoretical study, Phys. Rev. B **101**, 195414 (2020).

[21] T. P. T. Nguyen, S. A. Blundell, and C. Guet, Calculation of the biexciton shift in nanocrystals of inorganic perovskites, Phys. Rev. B **101**, 125424 (2020).

[22] T. P. T. Nguyen, A theoretical study of correlation effects of N electrons in semiconductor nanocrystals: Applications to optoelectronic properties of perovskite nanocrystals, Ph.D. thesis, Univ. Grenoble Alpes, France, 2020.

[23] P. C. Sercel, J. L. Lyons, N. Bernstein, and A. L. Efros, Quasicubic model for metal halide perovskite nanocrystals, J. Chem. Phys. **151**, 234106 (2019).

[24] J. Even, L. Pedesseau, and C. Katan, Analysis of multivalley and multibandgap absorption and enhancement of free carriers related to exciton screening in hybrid perovskites, J. Phys. Chem. C **118**, 11566 (2014).

[25] M. A. Becker, R. Vaxenburg, G. Nedelcu, P. C. Sercel, A. Shabaev, M. J. Mehl, J. G. Michopoulos, S. G. Lambrakos, N. Bernstein, J. L. Lyons, T. Stöferle, R. F. Mahrt, M. V. Kovalenko, D. J. Norris, G. Rainò, and A. L. Efros, Bright triplet excitons in caesium lead halide perovskites, Nature (London) **553**, 189 (2018).

[26] A. I. Ekimov, F. Hache, M. C. Schanneklein, D. Ricard, C. Flytzanis, I. A. Kudryavtsev, T. V. Yazeva, A. V. Rodina, and A. L. Efros, Absorption and intensity-dependent photoluminescence measurements on CdSe quantum dots—assignment of the 1st electronic-transitions, J. Opt. Soc. Am. B **10**, 100 (1993).

[27] J. D. Jackson, *Classical Electrodynamics*, 3rd ed. (Wiley, New York, 1998).

[28] Z. Wang (private communication).

[29] G. D. Mahan, *Many-Particle Physics*, 3rd ed. (Kluwer Academic, New York, 2000).

[30] A. V. Fedorov, A. V. Baranov, and K. Inoue, Two-photon transitions in systems with semiconductor quantum dots, Phys. Rev. B **54**, 8627 (1996).

[31] M. Kira and S. W. Koch, *Semiconductor Quantum Optics* (Cambridge University Press, New York, 2012).

[32] Z. Yang, A. Surrente, K. Galkowski, A. Miyata, O. Portugall, R. J. Sutton, A. A. Haghighirad, H. J. Snaith, D. K. Maude, P. Plochocka, and R. J. Nicholas, Impact of the halide cage on the electronic properties of fully inorganic cesium lead halide perovskites, ACS Energy Lett. **2**, 1621 (2017).

[33] D. N. Dirin, I. Cherniukh, S. Yakunin, Y. Shynkarenko, and M. V. Kovalenko, Solution-grown $CsPbBr_3$ perovskite single crystals for photon detection, Chem. Mater. **28**, 8470 (2016).

[34] J. Fu, Q. Xu, G. Han, B. Wu, C. H. A. Huan, M. L. Leek, and T. C. Sum, Hot carrier cooling mechanisms in halide perovskites, Nat. Commun. **8**, 1 (2017).

[35] P. Umari, E. Mosconi, and F. De Angelis, Relativistic GW calculations on $CH_3NH_3PbI_3$ and $CH_3NH_3SnI_3$ perovskites for solar cell applications, Sci. Rep. **4**, 4467 (2014).

[36] Z. G. Yu, Effective-mass model and magneto-optical properties in hybrid perovskites, Sci. Rep. **6**, 28576 (2016).

[37] M. C. Brennan, J. E. Herr, T. S. Nguyen-Beck, J. Zinna, S. Draguta, S. Rouvimov, J. Parkhill, and M. Kuno, Origin of the size-dependent stokes shift in $CsPbBr_3$ perovskite nanocrystals, J. Am. Chem. Soc. **139**, 12201 (2017).

[38] T. Takagahara, Excitonic optical nonlinearity and exciton dynamics in semiconductor quantum dots, Phys. Rev. B **36**, 9293 (1987).

[39] I. Lindgren and J. Morrison, *Atomic Many-Body Theory*, 2nd ed. (Springer, Berlin, 1986).

[40] I. Shavitt and R. J. Bartlett, *Many-Body Methods in Chemistry and Physics: MBPT and Coupled-Cluster Theory* (Cambridge University Press, Cambridge, 2009).

[41] L.-W. Wang, Real and spurious solutions of the $8 \times 8\,\mathbf{k}\cdot\mathbf{p}$ model for nanostructures, Phys. Rev. B **61**, 7241 (2000).